Analysis of images

In addition to the finite resolution, the camera system adds artefacts to the images owing to optical interference effects of the coherent illumination light and electronic crosstalk during readout of the CCD chip. In our case, the former results in a pattern of vertical stripes and the latter mainly creates a periodic noise with a wavelength of two pixels. As the phase and amplitude of both periodic distortions are not constant, they can not be cancelled by the normalization procedures and appear as periodic fluctuation in the noise correlation plot. Images with high amplitude of such fluctuations (visible outside the atom cloud) are removed from further analysis. The electronic noise is addressed after the determination of the correlation function, by convolving it with a horizontal three-pixel-wide gaussian mask for smoothing.

The correlation function as defined in equation (1) is obtained from a set of images as follows: from each image the autocorrelation function (ACF) is calculated by Fourier-transforming it, taking the absolute square to obtain the power spectral density and Fourier-transforming it back. Averaging the ACF of all images yields the numerator of equation (1), whereas the denominator is obtained by calculating the ACF of the average of all images.

Theoretical model

The origin of the correlation peaks can be understood as follows. Calculating the ACF determines the expectation value of the operator $\langle \hat{n}(\mathbf{x}_1,t)\,\hat{n}(\mathbf{x}_2,t)\rangle = \langle \hat{a}^+(\mathbf{x}_1,t)\,\hat{a}(\mathbf{x}_1,t)\,\hat{a}^+(\mathbf{x}_2,t)\,\hat{a}(\mathbf{x}_2,t)\rangle$ at time t, with $\mathbf{x}_1 = \mathbf{x} - \frac{1}{2}\mathbf{d}$, $\mathbf{x}_2 = \mathbf{x} + \frac{1}{2}\mathbf{d}$. The operators $\hat{a}(\mathbf{x},t)$ at position $\mathbf{x}$ and time t after release relate to the on-site operators $\hat{a}(\mathbf{r}_j)$ for the lattice sites j at positions $\mathbf{r}_j$ as

$$\hat{a}(\mathbf{x},t) = \sum_j w(\mathbf{x}-\mathbf{r}_j,t)e^{i(m/2\hbar t)(\mathbf{x}-\mathbf{r}_j)^2}\hat{a}(\mathbf{r}_j)$$

where w is the expanding wavefunction originally localized to the Wannier function at the site. For the product of Fock states representing the Mott insulator with site occupation n_i at site i, one finds

$$\left\langle \hat{a}^+(\mathbf{r}_k)\,\hat{a}^+(\mathbf{r}_m)\,\hat{a}(\mathbf{r}_l)\,\hat{a}(\mathbf{r}_n)\right\rangle = n_k\,n_m\,\delta_{kl}\delta_{mn} + n_k\,n_m\,\delta_{kn}\,\delta_{lm} \quad (4)$$

where the delta-term introduced through the normal ordering of the operators has been omitted. In the correlation function C, the first term in equation (4) will create a constant offset of 1 for large atom number N, whereas the second term introduces a spatial dependence in the correlations, leading to:

$$C_{3D}(\mathbf{d}) = C(\mathbf{x}_1-\mathbf{x}_2) = 1 + \frac{1}{N^2}\sum_{k,l} e^{i(m/\hbar t)(\mathbf{x}_1-\mathbf{x}_2)\cdot(\mathbf{r}_k-\mathbf{r}_l)} n_k n_l \quad (5)$$

Throughout the discussion, constant offsets of order $1/N$ are neglected compared to 1. For a regular one-dimensional lattice with unity filling and spacing a_{lat}, the sum can then be simplified to $1+\{[\sin^2(\pi N d/l)]/[N^2\sin^2(\pi d/l)]\}$, with $d = x_2 - x_1$ and $l = ht/(ma_{\mathrm{lat}})$, analogous to the optical interference created by a regular grating. In the limit of large N, this term corresponds to a series of peaks of height 1 and width l/N and converges to:

$$1 + \frac{1}{N}\sum_{j=-\infty}^{\infty}\delta(d/l - j)$$

For a regular three-dimensional system the structure term converges to:

$$C_{3D}(\mathbf{d}) = 1 + \frac{1}{N}\sum_j \delta((\mathbf{d} - \mathbf{p}_j\frac{t}{m})/l)$$

where $\mathbf{p}_j$ are the reciprocal three-dimensional lattice momenta. Because the imaging system registers only column densities and has a finite resolution, the operators $\hat{n}(\mathbf{x}_{1,2})$ both have to be convolved with the inverse point spread function (approximated as a gaussian of r.m.s. width σ) and integrated along the imaging axis before being evaluated. For unity filling this yields a smoothed two-dimensional correlation function:

$$C(\mathbf{d}) = 1 + \frac{1}{4\pi N}\left(\frac{l}{\sigma}\right)^2 \sum_j e^{-\{[\mathbf{d}-\mathbf{p}_j t/m]^2/4\sigma^2\}}$$

The heights of the peaks at the reciprocal lattice momenta therefore scale as $N^{-1}t^2$ for this simple homogeneous case. As indicated in the text, the N^{-1} scaling is modified to $N^{-0.64}$ for our harmonically trapped system by the appearance of Mott domains with filling factor larger than one for higher atom numbers. The prediction for the exponent has been obtained by numerically evaluating the sum in equation (5) using a model distribution of atoms in the lattice sites confined by a global parabolic potential. This distribution is predicted assuming the system can be described in the strongly interacting limit[30] with a local density approximation.

Received 27 January; accepted 28 February 2005; doi:10.1038/nature03500.

1. Hanbury Brown, R. & Twiss, R. Q. Correlation between photons in two coherent beams of light. *Nature* **177,** 27–29 (1956).
2. Henny, M. *et al.* The fermionic Hanbury Brown and Twiss experiment. *Science* **284,** 296–298 (1999).
3. Oliver, W. D., Kim, J., Liu, R. C. & Yamamoto, Y. Hanbury Brown and Twiss-type experiment with electrons. *Science* **284,** 299–301 (1999).
4. Kiesel, H., Renz, A. & Hasselbach, F. Observation of Hanbury Brown-Twiss anticorrelations for free electrons. *Nature* **418,** 392–394 (2002).
5. Bachor, H. A. & Ralph, T. C. *A Guide to Experiments in Quantum Optics* (Wiley-VCH, Weinheim, 2004).
6. Baym, G. The physics of Hanbury Brown-Twiss intensity interferometry: From stars to nuclear collisions. *Act. Phys. Pol. B* **29,** 1839–1884 (1998).
7. Altman, E., Demler, E. & Lukin, M. D. Probing many-body states of ultracold atoms via noise correlations. *Phys. Rev. A* **70,** 013603 (2004).
8. Jaksch, D., Bruder, C., Cirac, J. I., Gardiner, C. W. & Zoller, P. Cold bosonic atoms in optical lattices. *Phys. Rev. Lett.* **81,** 3108–3111 (1998).
9. Greiner, M., Mandel, O., Esslinger, T., Hänsch, T. W. & Bloch, I. Quantum phase transition from a superfluid to a Mott insulator in a gas of ultracold atoms. *Nature* **415,** 39–44 (2002).
10. Stöferle, T., Moritz, H., Schori, C., Köhl, M. & Esslinger, T. Transition from a strongly interacting 1D superfluid to a Mott insulator. *Phys. Rev. Lett.* **92,** 130403 (2004).
11. Hofstetter, W., Cirac, J. I., Zoller, P., Demler, E. & Lukin, M. D. High temperature superfluidity of fermionic atoms in optical lattices. *Phys. Rev. Lett.* **89,** 220407 (2002).
12. Kuklov, A. & Svistunov, B. Counterflow superfluidity of two-species ultracold atoms in a commensurate optical lattice. *Phys. Rev. Lett.* **90,** 100401 (2003).
13. Duan, L.-M., Demler, E. & Lukin, M. Controlling spin exchange interactions of ultracold atoms in an optical lattice. *Phys. Rev. Lett.* **91,** 090402 (2003).
14. Lewenstein, M., Santos, L., Baranov, M. A. & Fehrmann, H. Atomic Bose-Fermi mixtures in an optical lattice. *Phys. Rev. Lett.* **92,** 050401 (2004).
15. Roth, R. & Burnett, K. Quantum phases of atomic boson-fermion mixtures in optical lattices. *Phys. Rev. A* **69,** 021601(R) (2004).
16. Jurczak, C. *et al.* Atomic transport in an optical lattice: An investigation through polarization-selective intensity correlations. *Phys. Rev. Lett.* **77,** 1727–1730 (1996).
17. Yasuda, M. & Shimizu, F. Observation of two-atom correlation of an ultracold neon atomic beam. *Phys. Rev. Lett.* **77,** 3090–3093 (1996).
18. Kagan, Y., Svistunov, B. V. & Shlyapnikov, G. V. Effect of Bose condensation on inelastic processes in gases. *Sov. Phys. JETP Lett.* **42,** 209–212 (1985).
19. Burt, E. A. *et al.* Coherence, correlations, and collisions: What one learns about Bose-Einstein condensates from their decay. *Phys. Rev. Lett.* **79,** 337–340 (1997).
20. Laburthe-Tolra, B. *et al.* Observation of reduced three-body recombination in a correlated 1D degenerate Bose gas. *Phys. Rev. Lett.* **92,** 190401 (2004).
21. Grondalski, J., Alsing, P. M. & Deutsch, I. H. Spatial correlation diagnostics for atoms in optical lattices. *Opt. Exp.* **5,** 249–261 (1999).
22. Kolovsky, A. R. Interference of cold atoms released from an optical lattice. *Europhys. Lett.* **68,** 330–336 (2004).
23. Bach, R. & Rzazewski, K. Correlation functions of cold bosons in an optical lattice. *Phys. Rev. A* **70,** 063622 (2004).
24. Ketterle, W., Durfee, D. S. & Stamper-Kurn, D. M. in *Proc. Int. School of Physics "Enrico Fermi"* (eds Inguscio, M., Stringari, S. & Wieman, C. E.) 67–176 (IOS Press, Amsterdam, 1999).
25. Greiner, M., Bloch, I., Mandel, O., Hänsch, T. W. & Esslinger, T. Exploring phase coherence in a 2D lattice of Bose-Einstein condensates. *Phys. Rev. Lett.* **87,** 160405 (2001).
26. Hadzibabic, Z., Stock, S., Battelier, B., Bretin, V. & Dalibard, J. Interference of an array of independent Bose-Einstein condensates. *Phys. Rev. Lett.* **93,** 180403 (2004).
27. Batrouni, G. G. *et al.* Mott domains of bosons confined on optical lattices. *Phys. Rev. Lett.* **89,** 117203 (2003).
28. Naraschewski, M. & Glauber, R. Spatial coherence and density correlations of trapped Bose gases. *Phys. Rev. A* **59,** 4595–4607 (1999).
29. Greiner, M., Regal, C. A., Stewart, J. T. & Jin, D. S. Probing pair-correlated fermionic atoms through correlations in atom shot noise. Preprint at ⟨http://arxiv.org/cond-mat/0502411⟩ (2005).
30. Sheshadri, K., Krishnamurthy, H. R., Pandit, R. & Ramakrishnan, T. V. Superfluid and insulating phases in an interacting-boson model: mean-field theory and the RPA. *Europhys. Lett.* **22,** 257–263 (1993).

Acknowledgements We acknowledge discussions with E. Altman and M. Greiner, as well as financial support by the DFG, AFOSR and the EU under a Marie-Curie Fellowship (F.G.) and a Marie-Curie Excellence grant.

Competing interests statement The authors declare that they have no competing financial interests.

Correspondence and requests for materials should be addressed to I.B. (bloch@uni-mainz.de).

Orbital Kondo effect in carbon nanotubes

Pablo Jarillo-Herrero, Jing Kong*, Herre S.J. van der Zant, Cees Dekker, Leo P. Kouwenhoven & Silvano De Franceschi*

Kavli Institute of Nanoscience, Delft University of Technology, PO Box 5046, 2600 GA Delft, The Netherlands

* Present addresses: Department of Electrical Engineering and Computer Science, Massachusetts Institute of Technology, Cambridge, Massachusetts 02139-4307, USA (J.K.); Laboratorio Nazionale TASC-INFM, I-34012 Trieste, Italy (S.D.F.)

Progress in the fabrication of nanometre-scale electronic devices is opening new opportunities to uncover deeper aspects of the Kondo effect[1]—a characteristic phenomenon in the physics of strongly correlated electrons. Artificial single-impurity Kondo systems have been realized in various nanostructures, including semiconductor quantum dots[2–4], carbon nanotubes[5,6] and individual molecules[7,8]. The Kondo effect is usually regarded as a

spin-related phenomenon, namely the coherent exchange of the spin between a localized state and a Fermi sea of delocalized electrons. In principle, however, the role of the spin could be replaced by other degrees of freedom, such as an orbital quantum number[9,10]. Here we show that the unique electronic structure of carbon nanotubes enables the observation of a purely orbital Kondo effect. We use a magnetic field to tune spin-polarized states into orbital degeneracy and conclude that the orbital quantum number is conserved during tunnelling. When orbital and spin degeneracies are present simultaneously, we observe a strongly enhanced Kondo effect, with a multiple splitting of the Kondo resonance at finite field and predicted to obey a so-called SU(4) symmetry.

The simplest Kondo system consists of a localized, spin-$\frac{1}{2}$ electron coupled to a Fermi sea by means of a Heisenberg-like exchange interaction[1]. This simple system can be realized with a quantum dot (QD) device[2–4], which is a small electronic island connected to metallic leads via two tunnel barriers (see Fig. 1a). Below a characteristic temperature T_K, the so-called Kondo temperature, a many-body singlet state is formed between the QD spin and the surrounding conduction electrons (Fig. 1a). This state adds a resonant level at the Fermi energy of the electrodes, enabling the tunnelling of electrons across the QD. Such a Kondo resonance can lead to a strong enhancement of the conductance, overcoming the Coulomb blockade effect[2–4]. In principle, a Kondo effect might also occur in the absence of spin if another quantum number, for example an orbital degree of freedom, gives rise to a degeneracy (Fig. 1b). In this case, Kondo correlations lead to the screening of the local orbital 'polarization', and an orbital singlet is formed through a combination of orbital states. In the presence of both spin and orbital degeneracy, quantum fluctuations lead to a strong mixing of these two degrees of freedom (Fig. 1c). This increased degeneracy yields an enhancement of T_K (ref. 11). In the low-temperature limit, this system is described by a Hamiltonian obeying SU(4) symmetry, which implies that the spin and charge degrees of freedom are fully entangled and the state of the electron is represented by a four-component 'hyperspin'[12–15].

An orbital degeneracy is naturally expected in the electronic structure of carbon nanotubes[16] (CNTs). This degeneracy can intuitively be viewed to originate from the two equivalent ways in which electrons can circle around the graphene cylinder, namely clockwise and anticlockwise[17]. The rotational motion confers an orbital magnetic moment on the electrons. Consequently, the orbital degeneracy can be split by a magnetic field, B, parallel to the nanotube axis. (Experimental evidence for this effect, originally predicted by Ajiki and Ando[18], has recently been reported[17,19–21].) We label the orbital states of a CNT QD as $|+\rangle$ and $|-\rangle$ according to the sign of the energy shift that they experience under an applied B. Size quantization due to the finite CNT length results in two sets of orbital levels, $E_+^{(n)}$ and $E_-^{(n)}$, where $n = 1,2,3,\ldots$ is the quantization number. $E_+^{(n)} = E_-^{(n)}$ at $B = 0$ (assuming no orbital mixing), resulting in a fourfold degeneracy when including spin. The orbital and spin degeneracies are simultaneously lifted by a parallel B (Fig. 1d). The use of B permits the tuning of new degeneracies in connection with the crossing between levels from different shells. Here we are particularly interested in the crossing between states with the same spin polarization, of the type indicated by the yellow rectangle in Fig. 1d. We show below that the twofold orbital degeneracy originating from such a crossing gives rise to a purely orbital Kondo effect. We then consider the case of concomitant spin and orbital degeneracy at $B = 0$ (green rectangle in Fig. 1d) and present evidence for an SU(4) Kondo effect.

In a measurement of the linear conductance, G, as a function of gate voltage, V_G, the fourfold shell structure leads to consecutive groups of four closely spaced Coulomb blockade oscillations[6,22]. The B-evolution of such oscillations is shown in Fig. 2a for a CNT QD device (described in the inset to Fig. 2a and in the figure legend) in a V_G region encompassing two adjacent shells. Coulomb peaks (highlighted by green lines) appear as lines running from bottom to top and denote the sequential addition of electrons to the QD; the electron number increases from left to right. The observed pattern is explained in detail on the basis of the single-particle spectrum in Fig. 1d and taking into account the Coulomb interaction between electrons (see Supplementary Information).

The Coulomb peaks move to the left or right when increasing B,

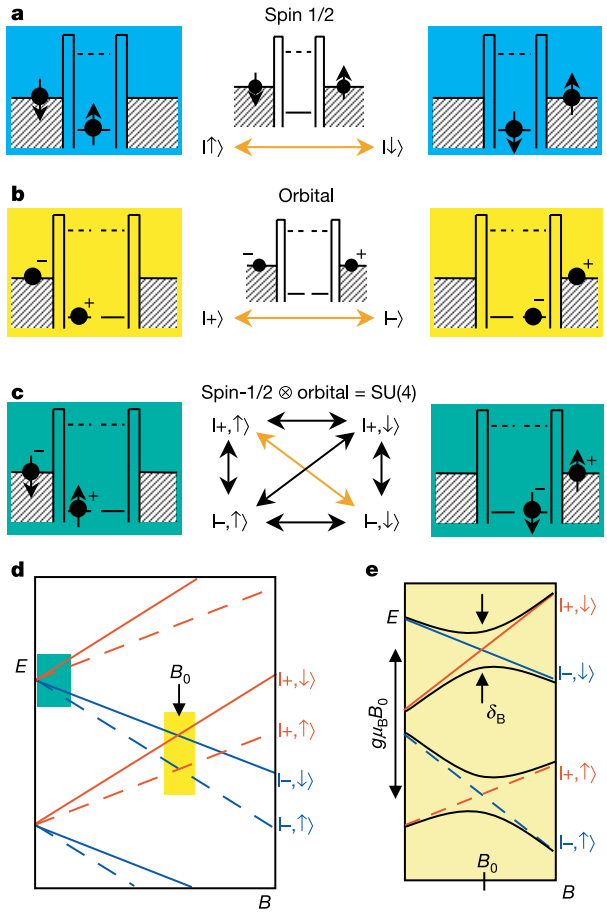

Figure 1 Spin, orbital and SU(4) Kondo effect in a quantum dot (QD) with an odd number of electrons. The left and right panels in **a**–**c** represent initial and final ground states, respectively. **a**, Schematic illustration of a spin-flip co-tunnelling process connecting the two states spin up, $|\uparrow\rangle$, and down, $|\downarrow\rangle$, from a single orbital state. The intermediate virtual state is shown in the central diagram. This co-tunnelling event is one of many higher-order processes that add up coherently, resulting in the screening of the local spin. **b**, Co-tunnelling process for spinless electrons for two degenerate orbital states, labelled $|+\rangle$ and $|-\rangle$. The depicted process flips the orbital quantum number from $|+\rangle$ to $|-\rangle$ and vice versa. The coherent superposition of orbital-flip processes leads to the screening of the local orbital quantum number. **c**, QD with two spin-degenerate orbitals leading to an overall fourfold degeneracy. Spin and/or orbital states can flip by one-step co-tunnelling processes, indicated by black arrows in the central diagram; the orange arrow refers to the co-tunnelling event connecting the two states depicted in the green diagrams. These processes lead to the entanglement of spin and orbital states, resulting in an enhanced SU(4) Kondo effect. **d**, Qualitative single-particle energy spectrum of a CNT QD in a magnetic field. Red and blue lines represent, respectively, orbital states shifting up, $|+\rangle$, and down, $|-\rangle$, in energy. Dashed and solid lines represent spin-up and spin-down states, respectively. The yellow rectangle highlights the region where a purely orbital Kondo effect can occur because of a level-crossing (at $B = B_0$) between spin-polarized states. The green rectangle highlights the SU(4) Kondo region. **e**, Close-up of the yellow rectangle in **d**. A finite coupling, δ_B, between $|+\rangle$ and $|-\rangle$ states causes an anticrossing (black lines). At high B, δ_B is smaller than the Zeeman splitting, $g\mu_B B$.

which corresponds to adding the last electron to a $|-\rangle$ or $|+\rangle$ orbital, respectively. When the ground-state configuration of the QD changes, kinks appear in the B-evolution of the Coulomb peaks. The two enhanced-conductance ridges at $B = B_0 \sim 6$ T, bounded by two such kinks and highlighted by dotted yellow lines, are due to the crossing between $|-\rangle$ and $|+\rangle$ states as described in Fig. 1d. A detailed analysis (see Supplementary Information) indicates that along these ridges the QD ground state is doubly degenerate, with the last added electron occupying the level crossing between $|+,\uparrow\rangle$ and $|-,\uparrow\rangle$ (left ridge) or between $|+,\downarrow\rangle$ and $|-,\downarrow\rangle$ (right ridge).

In the region near the degeneracy point, we are able to measure a small coupling between orbital states[21], resulting in level repulsion at $B = B_0$. The energy splitting is directly observed in the spectroscopy data of Fig. 2b, where the differential conductance, dI/dV, is shown as a function of B and bias voltage, V. In this measurement V_G and B are simultaneously varied to follow the middle of the Coulomb valley (dashed blue line in Fig. 2a). Here, single-electron tunnelling is suppressed and the spectroscopy is based on higher-order co-tunnelling processes, which lead to an enhancement of dI/dV every time that V equals an internal excitation energy[23]. We focus on the high-B region of Fig. 2b. As B is swept across B_0, the anticrossing between $|+,\downarrow\rangle$ and $|-,\downarrow\rangle$ (depicted in Fig. 1e) shows up in the two dI/dV ridges highlighted by dashed yellow lines. The level spacing, corresponding to half the distance between these lines, reaches a minimum value $\delta_B = 225\,\mu$V at $B = B_0 = 5.9$ T. In a measurement of dI/dV against (V,V_G) at 5.9 T, shown in Fig. 2c, the higher-order peaks appear as horizontal ridges inside the Coulomb diamond. Their spacing, $2\delta_B$, is independent of V_G, whereas their height increases towards the edges of the diamond.

An individual trace of dI/dV against V taken in the middle of the diamond is shown in Fig. 2d, together with traces measured at higher temperature, T. The strong overshoot of the dI/dV peaks and their log-T dependence (inset) indicate an important contribution from Kondo correlations. The observed behaviour is characteristic of a split Kondo resonance—that is, a Kondo resonance associated with two quasi-degenerate states—in line with recent theoretical predictions[24] and experiments[25]. It is important to note that the Zeeman spin splitting, $E_Z = g\mu_B B_0$, is three times δ_B, indicating that the Kondo effect originates entirely from orbital correlations occurring at the crossing between two spin-polarized states, $|+,\downarrow\rangle$ and $|-,\downarrow\rangle$. This conclusion is in agreement with the zero-field data that we show below. The large Zeeman splitting also ensures that the observed orbital Kondo resonance provides a conducting channel only for $|\downarrow\rangle$ electrons, thereby acting as a high-transmission spin filter[12–14]. In contrast, the conductance enhancement that occurs for three-electron shell filling originates from $|+,\uparrow\rangle$ and $|-,\uparrow\rangle$ states and hence it allows only the tunnelling of $|\uparrow\rangle$ electrons. Switching from one degeneracy to the other is controlled by simply switching the gate voltage, which then causes the CNT QD to operate as a bipolar spin filter.

We now centre our attention on the zero-field regime, in which both orbital and spin degeneracies are expected (green rectangle in Fig. 1d). The Coulomb oscillations corresponding to the filling of a single shell are shown in Fig. 3a for a different CNT QD device. The four oscillations are clearly visible at 8 K (red trace). At lower T, the conductance exhibits a pronounced enhancement in regions I and III—that is, for 1 and 3 electrons on the shell—and the corresponding Coulomb blockade valleys disappear completely at 0.3 K (black trace). This conductance enhancement is a hallmark of Kondo correlations. From the T-dependence (fully shown in the Supplementary Information) we estimate that $T_K = 7.7$ K, an unusually high value that can be ascribed to the enhanced degeneracy[11].

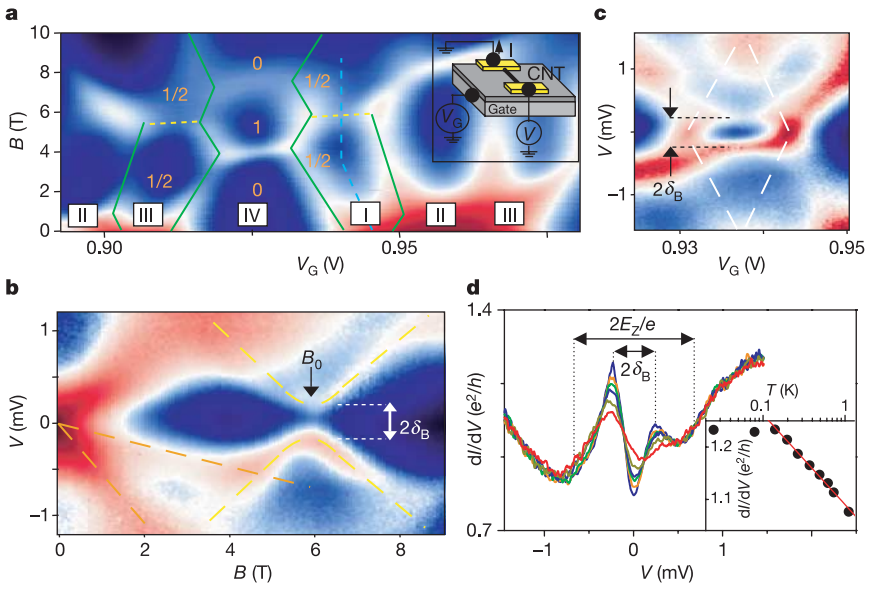

Figure 2 Orbital Kondo effect. **a**, Colour-scale representation of the linear conductance, G, versus B and V_G at $T \sim 30$ mK (G increases from dark blue to dark red). The green lines highlight the B-evolution of the Coulomb peaks. The dotted yellow lines highlight regions of enhanced conductance due to Kondo effect. Roman labels indicate the number of electrons on the last occupied shell near $B = 0$. Orange numbers indicate the spin of the ground state. Inset: device scheme. Carbon nanotubes were grown by chemical vapour deposition on p-type silicon substrates with a surface oxide 250 nm thick. Individual nanotubes were located by atomic force microscopy and contacted with Ti/Au electrodes (typical separation ~100–800 nm) defined by e-beam lithography. The highly doped silicon substrate was used as a back-gate. **b**, Colour-scale plot of the differential conductance, dI/dV, against V and B along the dashed blue line in **a**. The field splits the Kondo resonance into multiple peaks. The two orange lines highlight the evolution of the peaks associated with the spin and orbital splitting, respectively. The spectroscopy features are more pronounced for $V < 0$, most probably due to asymmetric tunnel barriers[30]. The yellow lines highlight the orbital anticrossing at $B = B_0 = 5.9$ T. **c**, Coulomb diamond for one electron on the last occupied shell at $B = 5.9$ T. **d**, Plot of dI/dV against V with varying T, from 25 mK (thick blue trace) to 1.1 K (thick red trace), at the anticrossing point ($B = 5.9$ T, $V_G = 937$ mV). Orbital splitting, δ_B, and Zeeman splitting, E_Z, are compared visually. The split Kondo peaks decrease with increasing T. Inset: plot of peak height against T evaluated for the left peak.

The important contribution of the orbital degree of freedom becomes apparent from the B-dependence of G (Fig. 3e, f). If this Kondo effect were determined by spin only (this could be the case if one of the orbitals was coupled weakly to the leads), G should decrease on a field scale $B \sim k_B T_K / g\mu_B \sim 6\,\mathrm{T}$ due to Zeeman splitting[26]. In contrast, G decays on a much smaller scale, $B \sim k_B T_K / 2\mu_{orb} \sim 0.5\,\mathrm{T}$, which is determined by the orbital splitting (an estimate of the orbital magnetic moment, μ_{orb}, is given below).

In the nonlinear regime, a single zero-bias Kondo resonance appears in regions I and III (Fig. 3b). Contrary to the result in Fig. 2c, no orbital splitting is observed because of the much larger T_K ($k_B T_K > \delta$ (refs 12, 13, 21)). In region II we observe two peaks at finite bias, reflecting the already known splitting of a singlet–triplet Kondo resonance[27]. To show that the Kondo resonance in regions I and III arises from simultaneous orbital and spin Kondo correlations, we investigate the effect of lifting spin and orbital degeneracies at finite B. As opposed to an ordinary spin-$\frac{1}{2}$ Kondo system (where the Kondo resonance splits in two peaks, separated by twice the Zeeman energy[3–9]) we find a fundamentally different splitting. At $B = 1.5\,\mathrm{T}$ (Fig. 3c), multiple split peaks appear in regions I and III as ridges of enhanced $\mathrm{d}I/\mathrm{d}V$ parallel to the V_G axis. In region I, the large zero-bias resonance opens up in four peaks that move linearly with B and become progressively smaller (Fig. 3d). The two inner peaks are due to Zeeman splitting, that is, to higher-order co-tunnelling from $|-,\uparrow\rangle$ to $|-,\downarrow\rangle$ ($|-\rangle$ is the lower-energy orbital). The two outer peaks arise from co-tunnelling from orbital $|-\rangle$ to orbital $|+\rangle$. In the latter case, inter-orbital co-tunnelling processes can occur either with or without spin flip. (However, the corresponding substructure[21] is not resolved owing to the broadening of the outer peaks.) Similar multiple splittings of the Kondo resonance have also been observed in several other samples. According to recent calculations[28], the observed multiple splitting of the Kondo resonance constitutes direct evidence of SU(4) symmetry, which implies the concomitant presence of spin as well as orbital Kondo correlations, confirming our previous finding.

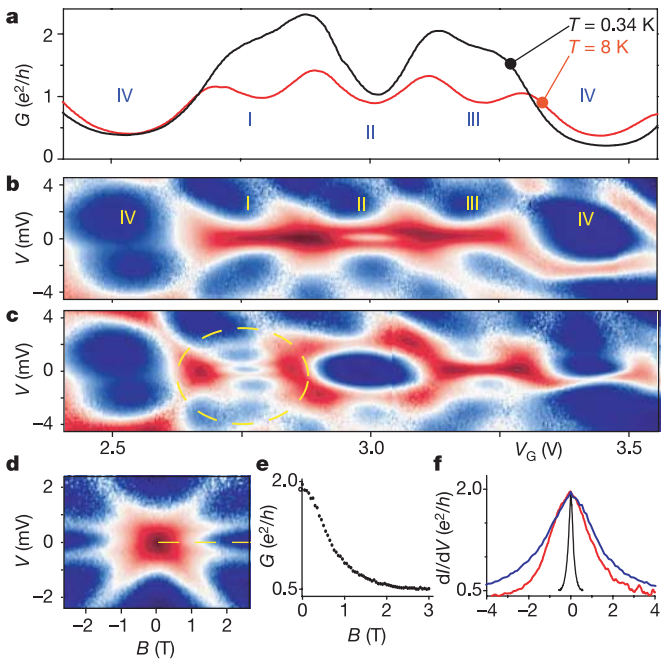

Figure 3 Kondo effect with combined spin and orbital degeneracies (spin⊗orbital Kondo effect). **a**, Plot of linear conductance, G, against V_G at $T = 8\,\mathrm{K}$ (red) and 0.34 K (black). **b**, Colour-scale plot of the differential conductance, $\mathrm{d}I/\mathrm{d}V$, against (V, V_G) at $T = 0.34\,\mathrm{K}$ and $B = 0$ ($\mathrm{d}I/\mathrm{d}V$ increases from blue to red). **c**, As in **b**, but at $B = 1.5\,\mathrm{T}$. The circle indicates the fourfold splitting in region I. **d**, Colour-scale plot of $\mathrm{d}I/\mathrm{d}V$ against (V,B) in the centre of Coulomb valley I. The Kondo peak appears as a bright spot at $(V,B) = (0,0)$, and splits into four peaks at finite B, following the simultaneous splitting of the orbital and spin states. **e**, B-dependence of G taken from the zero-bias dashed yellow line in **d**. G decreases on a ~0.5 T scale; that is, ~12-fold faster than expected from Zeeman splitting. **f**, Plot of G against normalized Zeeman energy, $g\mu_B B/k_B T_K$ (black trace), and against normalized orbital splitting, $2\mu_{orb}B/k_B T_K$ (blue trace). $T_K = 7.7\,\mathrm{K}$ as deduced from a fit of $G(T)$. (Note that $G(B) = 0.5G(0)$ when $2\mu_{orb}B/k_B T_K \sim 1$.) To compare the suppression due to B with that due to V, we also show a measurement of $\mathrm{d}I/\mathrm{d}V$ against normalized bias voltage, $eV/k_B T_K$ (red trace). The blue and red traces fall almost on top of each other, implying that lifting the orbital degeneracy suppresses the Kondo effect. This shows that the simultaneous degeneracy of orbital and spin states forms the origin of the strongly enhanced Kondo effect at $B = 0$.

The slope $|\mathrm{d}V/\mathrm{d}B|$ of a conductance peak (Fig. 3d) directly yields the value of the magnetic moment associated with the splitting. We obtain a spin magnetic moment $\mu_{spin} = \frac{1}{2}|\mathrm{d}V/\mathrm{d}B|_{spin} = 0.06\,\mathrm{meV\,T^{-1}} \sim \mu_B$ from the inner peaks, and an orbital magnetic moment $\mu_{orb} = \frac{1}{2}|\mathrm{d}V/\mathrm{d}B|_{orb}/\cos\varphi = 0.8\,\mathrm{meV\,T^{-1}} \sim 13\mu_B$ from the outer peaks (φ is the angle between the nanotube and B)[17]. The same value of μ_{orb} follows from the splitting of the Kondo resonance in region III (Fig. 3c). In this case, however, no Zeeman splitting is observed. Here, the magnetic field induces a transition from SU(4) to a spin-based SU(2) Kondo effect for which $k_B T_K$ remains larger than the Zeeman energy, hindering the splitting of the Kondo resonance up to a few teslas. Finally, we note that both the one-electron SU(4) and the two-electron singlet–triplet Kondo effects are characterized by a fourfold degeneracy, which results in an enhanced T_K (ref. 27). Apart from this, the two phenomena are fundamentally very different. The singlet–triplet Kondo effect is a spin phenomenon in which the role of the orbital degree of freedom is simply to provide the basis for the construction of spin-singlet and triplet two-particle states (see also Supplementary Information).

Because orbital Kondo correlations can arise only if the orbital quantum number is conserved during tunnelling, our experimental finding of orbital Kondo physics in CNT QDs raises an interesting question concerning the nature of the dot–lead coupling. In our devices, the metal contacts are deposited on top of the CNT and the QD is formed in the segment between them[29]. It is possible that when electrons tunnel out of the QD, they enter first the nanotube section underneath the contacts, where they dwell for some time before moving into the metal. Because the orbital quantum number is probably conserved in a CNT–CNT tunnel process, this intermediate step may account for the observed orbital Kondo effect. □

Received 22 November 2004; accepted 25 January 2005; doi:10.1038/nature03422.

1. Hewson, A. C. *The Kondo Problem to Heavy Fermions* (Cambridge Univ. Press, Cambridge, 1993).
2. Goldhaber-Gordon, D. *et al.* Kondo effect in a single-electron transistor. *Nature* **391,** 156–159 (1998).
3. Cronenwett, S. M., Oosterkamp, T. H. & Kouwenhoven, L. P. A tunable Kondo effect in quantum dots. *Science* **281,** 540–544 (1998).
4. Schmid, J., Weis, J., Eberl, K. & von Klitzing, K. A quantum dot in the limit of strong coupling to reservoirs. *Physica B* **256–258,** 182–185 (1998).
5. Nygård, J., Cobden, D. H. & Lindelof, P. E. Kondo physics in carbon nanotubes. *Nature* **408,** 342–346 (2000).
6. Buitelaar, M. R., Bachtold, A., Nussbaumer, T., Iqbal, M. & Schönenberger, C. Multi-wall carbon nanotubes as quantum dots. *Phys. Rev. Lett.* **88,** 156801 (2002).
7. Park, J. *et al.* Coulomb blockade and the Kondo effect in single-atom transistors. *Nature* **417,** 722–725 (2002).
8. Liang, W., Shores, M. P., Bockrath, M., Long, J. R. & Park, H. Kondo resonance in a single-molecule transistor. *Nature* **417,** 725–729 (2002).
9. Cox, D. L. & Zawadowski, A. Exotic Kondo effects in metals: magnetic ions in a crystalline electric field and tunnelling centers. *Adv. Phys.* **47,** 599–942 (1998).
10. Kolesnychenko, O. Yu., de Kort, R., Katsnelson, M. I., Lichtenstein, A. I. & van Kempen, H. Real-space imaging of an orbital Kondo resonance on the Cr(001) surface. *Nature* **415,** 507–509 (2002).
11. Inoshita, T., Shimizu, A., Kuramoto, Y. & Sakaki, H. Correlated electron transport through a quantum dot: the multiple-level effect. *Phys. Rev. B* **48,** 14725–14728 (1993).
12. Borda, L., Zaránd, G., Hofstetter, W., Halperin, B. I. & von Delft, J. SU(4) Fermi liquid state and spin filtering in a double quantum dot system. *Phys. Rev. Lett.* **90,** 026602 (2003).

13. Zaránd, G., Brataas, A. & Goldhaber-Gordon, D. Kondo effect and spin filtering in triangular artificial atoms. *Solid State Commun.* **126,** 463–466 (2003).
14. López, R. *et al.* Probing spin and orbital Kondo effects with a mesoscopic interferometer. Preprint available at ⟨http://xxx.lanl.gov/abs/cond-mat/0402361⟩.
15. Sasaki, S., Amaha, S., Asakawa, N., Eto, M. & Tarucha, S. Enhanced Kondo effect via tuned orbital degeneracy in a spin $\frac{1}{2}$ artificial atom. *Phys. Rev. Lett.* **93,** 017205 (2004).
16. Dresselhaus, M. S., Dresselhaus, G. & Eklund, P. C. *Science of Fullerenes and Carbon Nanotubes* (Academic, San Diego, 1996).
17. Minot, E., Yaish, Y., Sazonova, V. & McEuen, P. L. Determination of electron orbital magnetic moments in carbon nanotubes. *Nature* **428,** 536–539 (2004).
18. Ajiki, H. & Ando, T. Electronic states of carbon nanotubes. *J. Phys. Soc. Jpn.* **62,** 1255–1266 (1993).
19. Zaric, S. *et al.* Optical signatures of the Aharonov–Bohm phase in single-walled carbon nanotubes. *Science* **304,** 1129–1131 (2004).
20. Coskun, U. C., Wei, T.-C., Vishveshwara, S., Goldbart, P. M. & Bezryadin, A. *h*/*e* magnetic flux modulation of the energy gap in nanotube quantum dots. *Science* **304,** 1132–1134 (2004).
21. Jarillo-Herrero, P. *et al.* Electronic transport spectroscopy of carbon nanotubes in a magnetic field. Preprint available at ⟨http://xxx.lanl.gov/cond-mat/0411440⟩.
22. Liang, W., Bockrath, M. & Park, H. Shell filling and exchange coupling in single-walled carbon nanotubes. *Phys. Rev. Lett.* **88,** 126801 (2002).
23. De Franceschi, S. *et al.* Electron cotunneling in a semiconductor quantum dot. *Phys. Rev. Lett.* **86,** 878–881 (2001).
24. Paaske, J., Rosch, A. & Wölfle, P. Nonequilibrium transport through a Kondo dot in a magnetic field: perturbation theory. *Phys. Rev. B* **69,** 155330 (2004).
25. Pasupathy, A. N. *et al.* The Kondo effect in the presence of ferromagnetism. *Science* **306,** 86–89 (2004).
26. Costi, T. A. Kondo effect in a magnetic field and the magnetoresistivity of Kondo alloys. *Phys. Rev. Lett.* **85,** 1504–1507 (2000).
27. Sasaki, S. *et al.* Kondo effect in an integer-spin quantum dot. *Nature* **405,** 764–767 (2000).
28. Choi, M.-S., López, R. & Aguado, R. SU(4) Kondo effect in carbon nanotubes. *Phys. Rev. Lett.* (submitted).
29. Mann, D., Javey, A., Kong, J., Wang, Q. & Dai, H. J. Ballistic transport in metallic nanotubes with reliable Pd ohmic contacts. *Nano Lett.* **3,** 1541–1544 (2003).
30. Bonet, E., Deshmukh, M. M. & Ralph, D. C. Solving rate equations for electron tunneling via discrete quantum states. *Phys. Rev. B* **65,** 045317 (2002).

Supplementary Information accompanies the paper on **www.nature.com/nature**.

Acknowledgements We thank G. Zaránd, R. Aguado and J. Martinek for discussions. Financial support was obtained from the Japanese Solution Oriented Research for Science and Technology (SORST) program and the Dutch Fundamenteel Onderzoek der Materie (FOM).

Competing interests statement The authors declare that they have no competing financial interests.

Correspondence and requests for materials should be addressed to P.J. (pablo@qt.tn.tudelft.nl).

Compact, stable and efficient all-fibre gas cells using hollow-core photonic crystal fibres

F. Benabid, F. Couny, J. C. Knight, T. A. Birks & P. St J. Russell

Photonics and Photonic Materials Group, Department of Physics, University of Bath, Bath BA2 7AY, UK

Gas-phase materials are used in a variety of laser-based applications—for example, in high-precision frequency measurement[1,2], quantum optics and nonlinear optics[3,4]. Their full potential has however not been realized because of the lack of a suitable technology for creating gas cells that can guide light over long lengths in a single transverse mode while still offering a high level of integration in a practical and compact set-up or device. As a result, solid-phase materials are still often favoured, even when their performance compares unfavourably with gas-phase systems. Here we report the development of all-fibre gas cells that meet these challenges. Our structures are based on gas-filled hollow-core photonic crystal fibres, in which we have recently demonstrated substantially enhanced stimulated Raman scattering[5,6], and which exhibit high performance, excellent long-term pressure stability and ease of use. To illustrate the practical potential of these structures, we report two different devices: a hydrogen-filled cell for efficient generation of rotational Raman scattering using only quasi-continuous-wave laser pulses; and acetylene-filled cells, which we use for absolute frequency-locking of diode lasers with very high signal-to-noise ratios. The stable performance of these compact gas-phase devices could permit, for example, gas-phase laser devices incorporated in a 'credit card' or even in a laser pointer.

Our all-fibre gas cells consist of hollow-core photonic crystal fibre (HC-PCF) filled with gas and spliced hermetically at both ends to standard single-mode optical fibre (SMF) (Fig. 1a, d). These novel devices have no bulk-optics components, and may be used with a wide range of commercially available optical fibre components (such as couplers, filters, mirrors and lasers). Moreover, the use of HC-PCF in which light is guided in a single transverse mode by means of a photonic bandgap created in the 'photonic crystal' cladding[7] greatly increases the efficiency of these laser–gas devices[5,6].

The high air-filling fraction of the HC-PCFs (which are formed by a network of glass webs typically just a few hundred nanometres thick) makes it very challenging to fusion-splice these fibres without collapsing and deforming the microstructure, which would give a high insertion loss. It is also important to avoid contaminating the PCF with solid deposits and water. Nevertheless, after some practice, routine splicing of HC-PCF to SMF was achieved with a typical loss of 1–2 dB. We estimate that a perfect splicing procedure using our fibres would yield a loss of 0.6–0.8 dB. Of this, 0.15 dB arises from the refractive index mismatch between the fibre cores, and is therefore fundamental. The rest is due to modal field mismatch, which we estimate by the butt-joint approximation[8] to be 0.4–0.6 dB. The discrepancy between estimated and achieved splice losses is linked to the formation of a recess in the end face of the HC-PCF when heated in the splicer (Fig. 1b). We believe this results from the action of surface tension along the many glass–air interfaces within the holey structure, the viscosity of which offers much less resistance to deformation than the solid glass in the outer cladding of the fibre. The mechanical strength of the splices is

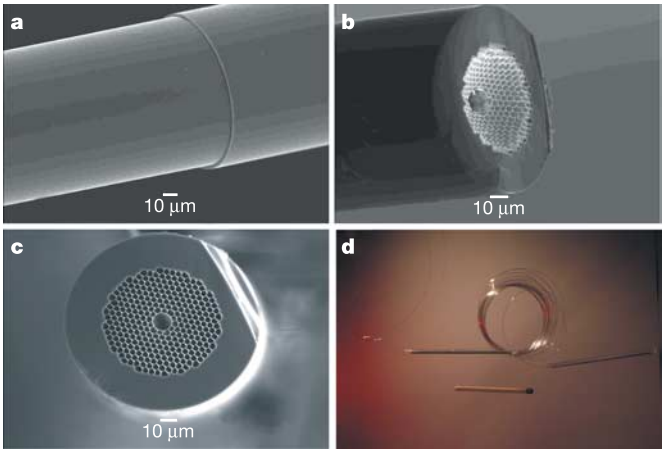

Figure 1 HC-PCF-based gas-cell assembly. **a**–**c**, Images obtained using a scanning electron microscope. **a**, Side view of a 1,550 nm HC-PCF (the narrower fibre) spliced to an SMF. **b**, End view of an HC-PCF cleaved at the junction of the splice. The recess, which creates an air gap of a few tens of micrometres between the fibre cores, is due to the action of surface tension during fusion. **c**, View of the same piece of HC-PCF as in **a** and **b** but cleaved a few millimetres from the splice, showing clearly the preservation of the microstructural integrity. **d**, Photograph of a 5-m-long hydrogen-filled HC-PCF gas cell, showing its size compared to that of a match.